

Nanoporous Tin with a Granular Hierarchical Ligament Morphology as a Highly Stable Li-Ion Battery Anode

John B. Cook,^{†,⊥} Eric Detsi,^{†,⊥} Yijin Liu,^{||} Yu-Lun Liang,[†] Hyung-Seok Kim,[‡] Xavier Petrisans,[‡] Bruce Dunn,^{‡,§} and Sarah H. Tolbert^{*,†,‡,§}

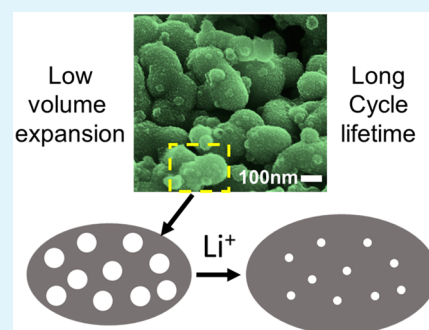
[†]Department of Chemistry and Biochemistry, [‡]Department of Materials Science and Engineering, and [§]The California NanoSystems Institute, University of California, Los Angeles, Los Angeles, California 90095, United States

^{||}Stanford Synchrotron Radiation Lightsource, SLAC National Accelerator Laboratory, Menlo Park, California 94025, United States

Supporting Information

ABSTRACT: Next generation Li-ion batteries will require negative electrode materials with energy densities many-fold higher than that found in the graphitic carbon currently used in commercial Li-ion batteries. While various nanostructured alloying-type anode materials may satisfy that requirement, such materials do not always exhibit long cycle lifetimes and/or their processing routes are not always suitable for large-scale synthesis. Here, we report on a high-performance anode material for next generation Li-ion batteries made of nanoporous Sn powders with hierarchical ligament morphology. This material system combines both long cycle lifetimes (more than 72% capacity retention after 350 cycles), high capacity (693 mAh/g, nearly twice that of commercial graphitic carbon), good charging/discharging capabilities (545 mAh/g at 1 A/g, 1.5C), and a scalable processing route that involves selective alloy corrosion. The good cycling performance of this system is attributed to its nanoporous architecture and its unique hierarchical ligament morphology, which accommodates the large volume changes taking place during lithiation, as confirmed by synchrotron-based ex-situ X-ray 3D tomography analysis. Our findings are an important step for the development of high-performance Li-ion batteries.

KEYWORDS: nanoporous metal, porous materials, tin, high capacity anode, transmission X-ray microscopy, TXM, alloy anode



1. INTRODUCTION

Commercialization of the first Li-ion batteries in 1991 was made possible by what people called rocking chair technology, which utilized LiCoO₂ and graphite electrodes.^{1,2} Twenty-five years later, graphite is still used as a negative electrode in the majority of Li-ion batteries. The success of graphitic carbon electrodes is attributed to its high electronic conductivity, low volume change during cycling, and long cycle lifetime.^{3–5} However, its relatively low gravimetric and volumetric theoretical capacities of 372 mAh/g and 756 mAh/cm³ limit the use of graphite in Li-ion batteries for long-range electric vehicles and many miniaturized portable electronics devices.⁶ These new advanced applications undeniably require materials with higher energy storage densities than what graphite can provide. Among alternative anode materials, tin and its neighbor in the periodic table, Si, are attractive candidates for their high Li storage capacity. Sn has theoretical gravimetric and volumetric Li storage capacities of 990 mAh/g and 1991 mAh/cm³, while Si has an even higher gravimetric capacity of 3579 mAh/g.⁶ The volumetric capacities of Si and Sn are comparable, however (Si volumetric capacity is 2190 mAh/cm³),⁸ and this metric is more important than gravimetric capacity for applications with space constraints (e.g., electric vehicles, laptops, cell phones, etc.). Although the volumetric capacities of Sn and Si are similar, Sn has the additional benefit

of a much higher electrical conductivity than silicon because it is a metal, making it the ideal choice for Li-ion battery anodes. Unfortunately, as with many high-capacity anode materials, the alloying reaction of Sn or Si with Li is associated with extreme volume changes (~300%) between the initial and final states.^{7–14} This expansion is thought to be responsible for the electrode failure of bulk, micrometer-sized tin and Si particles after just a few cycles. One significant failure mechanism is crack propagation and pulverization of the active electrode material leading to electrically isolated fragments that no longer contribute to the total capacity of the electrode.^{9,10,15}

The above-mentioned cell failure and corresponding short battery lifetimes represent the main challenge in this field, and this issue has significantly delayed the development of high-performance Sn anodes for Li-ion batteries. As a result, despite the fact that various nanostructured forms of Sn have recently been shown to significantly outperform graphitic carbon in terms of theoretical capacity,^{16–18} developing a high capacity nanostructured Sn anode with good cycle life remains a major challenge. Even small Sn nanocrystals have been shown to suffer from the deleterious effects of extreme volume changes

Received: July 26, 2016

Accepted: December 7, 2016

Published: December 7, 2016

during cycling. For example, a recent transmission electron microscopy study showed that even extremely small 10 nm monodispersed Sn nanocrystals undergo pulverization as a result of Li-induced volume changes.¹⁹ However, in some cases, reasonable capacity retention can be achieved even with nanocrystal-based electrodes. For example, ~40 nm Sn nanocrystals were evaluated as Li-ion battery electrodes, achieving ~80% capacity retention over 70 cycles.²⁰ Nanostructures with varying complexities like carbon encapsulated Sn nanoparticles,^{21,22} SnO₂@C yolk-shell spheres,²³ and carbon Sn composites²⁴ have also shown varying degrees of success. While some of these more complicated nanostructured graphene composites and tin oxide materials show improved cycle lifetimes, pure metallic tin structures still show limited cycle lifetimes.^{16–18,25–27}

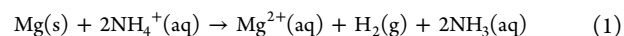
It is clear that nanostructuring tin offers benefits as compared to bulk micrometer tin powders, but those approaches do not fully alleviate the damaging effects caused by repeated volume change during cycling. The next step, in an effort to increase the cycle lifetimes of tin, may be the development of porous architectures. While long cycle lifetimes have not yet been demonstrated in porous tin metal, much work has been done on other porous alloy-type materials including silicon^{28–31} and tin oxide.^{25–27} Understanding the failures and successes of those systems can be leveraged, and applied, to the porous tin under investigation in this study. The volume change in Si during electrochemical lithiation is comparable to that of Sn, and various porous silicon architectures have been shown to increase cycle lifetimes up to 300 cycles.^{28,31} In addition, nanoporous tin oxide shows favorable cycling characteristics; however, porous tin oxides still suffer from extremely low first cycle efficiencies typically of only ~40–50% due to the irreversible conversion of SnO₂ to form Sn and Li₂O.^{27–29} Pure nanoporous tin metal, on the other hand, should have higher first cycle efficiencies than SnO₂, while also benefiting from the longer cycle lifetimes associated with these porous nanoscale architectures.

One facile synthetic route to nanoporous metals is dealloying,^{32,33} a top-down nanosynthesis technique where the most chemically active element is selectively removed from a dense parent alloy using acidic or alkaline aqueous electrolytes,^{34–38} often in combination with a bias voltage.^{39,40}

Porosity evolution in tin metal was recently investigated by Chen and Sieradzki during dealloying of Li–Sn alloys with various compositions.⁴¹ They reported on nanoporous tin with the standard nanowire-like ligament morphology.⁴¹ In our preliminary work, we have found that nanoporous tin with such a nanowire-like ligament morphology does not exhibit long cycle lifetimes when used as an anode material in Li-ion batteries. As a result, in this work, we aim at developing nanoporous tin (NP-Sn) with a different ligament morphology. Moreover, our goal is to directly produce nanoporous tin in powder form, rather than a monolithic piece of nanoporous metal, so that the NP-Sn powder can be directly integrated into composite electrodes using commercial battery electrode processing techniques. Finally, another important requirement for commercial battery electrodes is that the processing procedure should be low-cost and easily applicable for large-scale synthesis, and we have tried to incorporate those ideas since the inception of this work.

Mechanically stable, monolithic nanoporous metals are made by limiting the content of the sacrificial element in the parent alloy to between 60 and 75 at. %.^{32,34,36,42} For the present work,

we are interested in micrometer-sized grains of porous Sn. Therefore, we use parent alloys with high sacrificial element content (>80 at. % Mg) to promote fragmentation of the NP-Sn during dealloying. Similar effects have been reported previously for nanoporous silver (NP-Ag) made by selective removal of aluminum from Ag–Al parent alloys with compositions in the range between Ag₁₅Al₈₅ and Ag₅Al₉₅ at. %.³⁵ Material fragmentation and pulverization during dealloying is caused by the poor mechanical stability of dealloyed structures when more than 85 at. % of sacrificial Al was removed,³⁵ and also by the high density of hydrogen gas released during Al dissolution.³⁵ Similarly, in the present work, the high content of sacrificial Mg and the large amount of H₂ gas released during the selective corrosion of Mg, according to eq 1, help break up the NP-Sn, resulting in a micrometer-sized NP-Sn powder after dealloying.



The dealloying reaction is favorable, as indicated by calculated changes in enthalpy, entropy, and free energy for the reaction in eq 1. Values are $\Delta H = -362.41$ kJ/mol, $\Delta S = -44.41$ J/mol-K, and $\Delta G = -349.18$ kJ/mol. The reaction is enthalpically downhill, dominated by the enthalpy of oxidizing Mg to Mg²⁺. The entropy change is slightly negative, which is unfavorable. This somewhat counterintuitive fact results because of the large negative entropy of solvation of Mg²⁺, which interacts strongly with water and dramatically reduces the water entropy. Any release of the ammonia gas can be neglected because the solubility of ammonia in water is very high (around 16 M, 33% w/w, or 2.64 mol/100 g of water). Overall, the reaction is highly favorable, with the large negative free energy change dominated by the enthalpy of Mg oxidation.

We next consider the viability of large-scale fabrication of NP-Sn using our method. While the large content of sacrificial Mg (85 at. %) may seem wasteful, the Mg can be recovered by Mg electrowinning, an affordable process used to both electrochemically recycle and extract Mg from its ores. Moreover, a precursor alloy with 85 at. % Mg is only 54 wt % Mg, and the cost of Mg per kg is about 1/10th the cost of Sn. As a result, from a materials point of view, the large content of sacrificial Mg is not economically prohibitive. Moreover, many nanomaterials synthesis methods involve high energy and high cost reagents such as SnCl₄. As compared to reagents like this, the added cost required to recover magnesium is small. While there are costs associated with all of the processing steps, the method proposed here appears to be much more scalable than many nanomaterials synthesis methods.

Here, we thus use these methods to report on a novel NP-Sn powder made by selective dealloying with ligaments that are composed of very small Sn grains. We use a Sn–Mg binary system with composition Sn₁₅Mg₈₅ at. % as the precursor to this NP-Sn. Using synchrotron-based transmission X-ray microscopy (TXM), we show that this novel NP-Sn structure is ideal for accommodating the large volume change associated with electrochemical lithium alloying. In agreement with those ideas, we also demonstrate that NP-Sn has attractive energy storage properties, high capacity, good cycle lifetimes, and favorable kinetic performance.

2. EXPERIMENTAL SECTION

2.1. Synthesis of Nanoporous Sn Powder. A Sn₁₅Mg₈₅ at. % master alloy was made by melting pure Sn (1 N, Alfa Aesar) and Mg (1 N, Alfa Aesar) at 700 °C in a graphite boat, using a quartz tube

under argon flow. The Mg content of the precursors used to synthesize the master alloy was about 10% higher than the desired content to compensate for Mg evaporation during melting. The metals were heated to 700 °C, and then the melt was mixed for about 5 min by repeated mechanical shaking of the graphite boat. The amount of Mg that evaporated during the melting process was tracked using the loss of weight of the master alloy. Heating was stopped when the desired weight loss from the master alloy as a result of Mg evaporation was achieved (i.e., after evaporation of the excess ~10% Mg). The as-synthesized alloy was brittle and displayed a purple color. In a typical synthesis procedure, the final weight of our Sn₁₅Mg₈₅ at. % parent alloy was ~2.5 g, and the corresponding amount of NP-Sn generated during dealloying was ~1.1 g. We emphasize that, with respect to scaling up the processing, the amount of parent alloy (2.5 g) was only restricted by the size of the graphite boat; the procedure is easily scalable for the synthesis of a large amount of NP-Sn.

Mg was selectively removed from the above ~2.5 g of Sn₁₅Mg₈₅ at. % parent alloy by free-corrosion dealloying in 300 mL of 1 M ammonium sulfate.^{43,44} During dealloying, the initially colorless ammonium sulfate solution turns dark gray or black within a few minutes as the parent alloy begins to break apart and the powder disperses in the solution. The color of the solution (dark gray or black) depends on the exact size of the micrometer-scale NP-Sn powder grains, and thus on the Mg:Sn ratio. After a few minutes, the dark gray solution containing dispersed NP-Sn powder was decanted to separate from the unreacted Sn/Mg parent alloy, and diluted 2× (or more) with DI water to limit the coarsening of the freshly dealloyed NP-Sn powder. Another 300 mL of 1 M ammonium sulfate was then added to the original piece of parent alloy, and the process was repeated multiple times until the Sn/Mg parent alloy was fully dealloyed.

Powders were collected by simple gravity sedimentation, the diluted ammonium sulfate solution was decanted, and the powders were washed several times with DI water until the pH was 7. After being washed, energy dispersive X-ray spectroscopy (EDS) analysis of the NP-Sn particles did not show any trace of sulfur (S) from the ammonium sulfate.

2.2. Electrode Preparation and Electrochemical Studies. The anode was similar to those used previously for Si, and was made from a slurry consisting of 66 wt % NP-Sn powder, used as the active component for Li storage, 16 wt % vapor grown carbon fibers (Sigma-Aldrich), used as conductive additive, and 18 wt % carboxymethyl cellulose ($M_w = 250$ K, Sigma-Aldrich), used as binder.⁴⁵ The electrode components were mixed together with water by ball-milling to obtain a homogeneous thick paste. The slurry was then cast on 9 μm copper foil (MTI Corp), dried at ambient temperature for 1 h, and further dried at 70 °C under vacuum overnight to evaporate the excess solvent. The mass loading of the electrode was ~1 mg/cm² of active material. These electrodes were assembled into 2016 coin cells using lithium metal as the counter electrode, glass fiber (Watman) as the separator, and 1 M LiPF₆ in a 1:1 ethylene carbonate/dimethylcarbonate solvent (Sigma-Aldrich) with 5% (v/v) fluorinated ethylene carbonate (TCI America) as the electrolyte. Half-cell cycling was studied between 0.07 and 1.0 V (vs Li/Li+) using an Arbin BT-2000. Electrochemical impedance spectroscopy was carried out on a VSP potentiostat/galvanostat (Bio-Logic). The impedance measurements were performed on two-electrode coin cells between 900 kHz and 100 mHz using a 10 mV signal. Impedance data were collected at 1 V after each deinsertion cycle. A 60 s rest was applied before each impedance measurement, during which time the voltage of the cell dropped from 1000 to ~950 mV. The 1C rate is defined as 650 mA/g.

2.3. Structural Characterizations. Powder X-ray diffraction (XRD) was performed in a PANalytical X'Pert Pro operating with Cu K α ($\lambda = 1.5418$ Å) using a 0.03° step size, a voltage of 45 kV, and a current of 40 mA. XRD patterns were recorded in the range of 10° < 2 θ < 80°. Transmission electron microscopy (TEM) was performed using a FEI Technai T12 operating at 120 kV. Nitrogen porosimetry was carried out using a Micromeritics TriStar II 3020. The surface area was calculated from the adsorption branch of the isotherm between 0.04 and 0.30 P/P^0 using the Brunauer–Emmett–Teller (BET) model. The pore diameter and pore volume were also calculated from

the adsorption branch of the isotherm using the Barret–Joyner–Halenda (BJH) model. X-ray photoelectron spectroscopy (XPS) analysis was performed using a Kratos Axis Ultra DLD with a monochromatic Al (K α) radiation source. The charge neutralizer filament was used to control charging of the sample, a 20 eV pass energy was used with a 0.1 eV step size, and scans were calibrated by shifting the C 1s peak to 284.8 eV. Integrated peak areas and atomic ratios were found using the CasaXPS software. The atomic sensitivity factors used were from the Kratos library within the Casa software.

Transmission X-ray microscopy was performed at beamline 6-2C of the Stanford Synchrotron Radiation Lightsource (SSRL) at the SLAC National Accelerator Laboratory. X-rays at 7 keV were used to perform nondestructive investigation of the electrode morphology at the nano/meso scale. The electrodes were washed with dimethylcarbonate solvent and were dried in vacuum. The electrode samples were then peeled off the metal current collector to avoid unnecessary absorption of the X-rays by the copper foil. The samples were kept in steady helium flow during the measurement to avoid oxidation by air and to mitigate heat load from the focused X-ray illumination. Projection images were collected over an angular range of 180° with a step size of 1°. 3D volumes at about 16 × 20 × 30 μm^3 were reconstructed with a voxel size at 27.3 × 27.3 × 27.3 nm³ using the in-house developed software package known as TXM-Wizard.⁴⁶

3. RESULTS AND DISCUSSION

3.1. Microstructural and Phase Characterizations. The EDS spectra of the parent alloy before and after dealloying are shown in Figure 1a and b. In Figure 1b, the intense Mg signal and moderate intensity oxygen signal (likely mostly from MgO), both observed in Figure 1a, have almost entirely vanished as a result of the dealloying process. Quantitative elemental analysis reveals that the residual Mg content in NP-Sn is below 5 at. %. While quantitative oxygen analysis can be challenging using EDS because of the low X-ray energy, qualitative analysis is robust and the data here clearly indicate that little oxide remains in the dealloyed material.

Figure 1c shows the XRD pattern of the parent alloy before (black) and after (blue) dealloying. The dominant phase in the parent alloy corresponds to the Mg₂Sn intermetallic compound, and the calculated Scherrer size of this phase is 60 nm. This crystalline phase nearly vanishes after dealloying, resulting in NP-Sn that crystallizes in the standard tetragonal β -Sn structure (141/*amd* space group) matching JCPDS card number 00-004-0673. The Scherrer size of the β -Sn is smaller than the parent alloy, and is calculated to be 30 nm. The small amount of remaining Mg₂Sn present in the final product has a calculated Scherrer size of ~30 nm, which indicates that any remaining intermetallic phase is not typical of the starting alloy and may be trapped in small solvent inaccessible pockets.

The low magnification scanning electron micrograph (SEM) in Figure 2a shows the microstructure of the NP-Sn powder dispersed on a carbon substrate. The as-synthesized particles have random shapes and sizes in the sub-10 μm range, which we attribute to the material fragmentation during dealloying. Mg and Sn form an intermetallic phase with stoichiometry Mg₂Sn corresponding to a composition of Sn₃₃Mg₆₇ at. % (see Sn–Mg phase diagram in Figure S1). For this work, we purposefully increased the Mg content from 67% to 85% to form some nearly pure Mg microdomains in the parent alloy. Fragmentation of the dealloyed materials into micrometer scale grains (i.e., into a NP-Sn powder) is then facilitated when these domains are etched away during dealloying.

The high magnification SEM of these particles shows that they are indeed porous (see Figure 2b). While the porous architecture in the NP-Sn is disordered, a common feature in

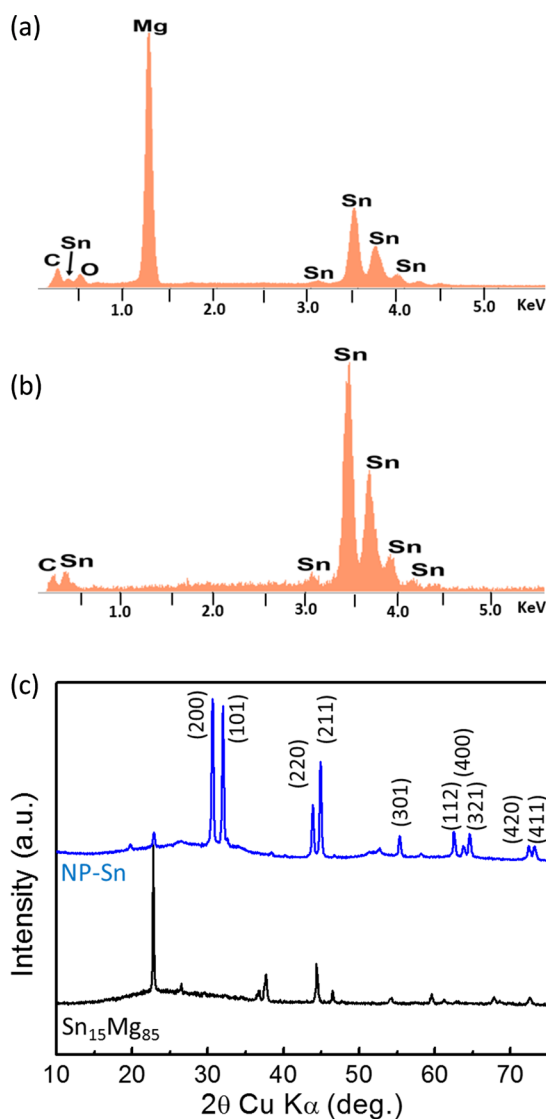


Figure 1. EDS spectrum of the $\text{Sn}_{15}\text{Mg}_{85}$ parent alloy before dealloying (a). EDS spectrum of NP-Sn after dealloying showing that the magnesium signal vanishes as a result of the dealloying process (b). X-ray diffraction patterns of the parent alloy before dealloying (black) and of NP-Sn after dealloying (blue) (c). The dominant crystalline phase after dealloying is β -tin.

most nanoporous metals,^{32,35,36,38,39,41,42,47,48} the ligaments exhibit a granular morphology (see Figure 2c) rather than interpenetrating nanowire type morphology commonly found in dealloyed nanoporous metals.^{32,35,36,38,39,41,42,47,48} The average ligament diameter varies between ~ 100 and ~ 200 nm. The small-scale structure of the ligaments was further characterized by TEM as shown in Figure 3a–c. It can clearly be seen from these TEM micrographs that the ligaments consist of clustered ~ 5 nm Sn nanocrystals (Figure 3c). This hierarchical structure is very well suited to accommodating volume change, and undergoing fast electrochemical reactions throughout the cycling process.

3.2. Nitrogen Adsorption Experiments. Nitrogen adsorption experiments were performed to confirm the presence of porosity in the dealloyed NP-Sn powder. NP-Sn exhibits a type II N_2 adsorption–desorption isotherm, with hysteresis occurring above $0.6 P/P_0$ (Figure S2a). This type of adsorption behavior is indicative of a material with both

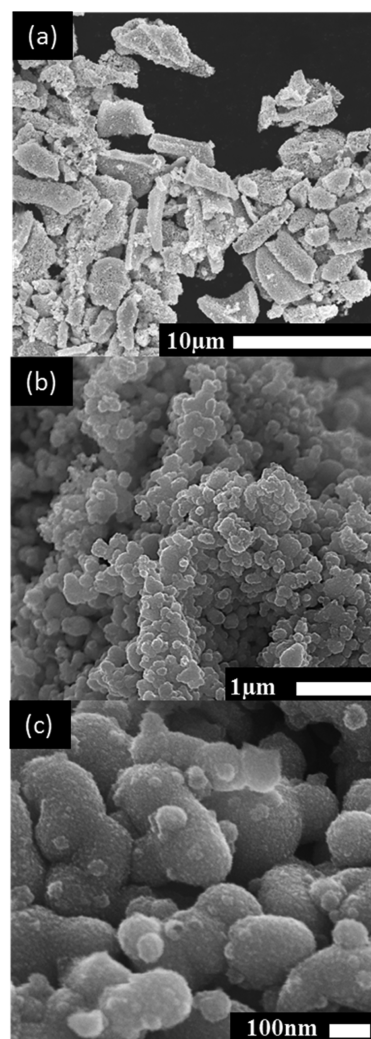


Figure 2. Scanning electron microscopy images of NP-Sn at different magnifications (a–c). Low magnification image of as-synthesized NP-Sn powder indicates that it consists of randomly shaped NP-Sn grains with sizes in the sub- $10\ \mu\text{m}$ range. The higher magnification images show the porous nanostructure, which consists of 100 – 300 nm ligaments and pores.

mesopores and macropores. The calculated BET surface area is $19\ \text{m}^2/\text{g}$. Surface area is an extremely important metric for alloy type anode materials because formation of the solid electrolyte interphase (SEI) occurs at the surface, and that surface film can greatly affect the performance characteristics. We speculate that the surface area of our NP-Sn is nearly optimal, in that the charge transfer rate is increased by increasing the flux of Li-ions at the surface, without the risk of extreme amounts of SEI being formed due to very large surface areas. The average pore size calculated from the Barret–Joyner–Halenda (BJH) model using the adsorption isotherm (Figure S2b) is ~ 70 nm with a total pore volume of $0.045\ \text{cm}^3/\text{g}$. Using that pore volume, the percent porosity of NP-Sn is estimated to be 25%. As shown later, this open porous system combined with the granular ligament morphology is incredibly good at accommodating the cycling induced volume change of $\sim 300\%$, taking place when the NP-Sn powder is electrochemically alloyed with Li.

3.3. X-ray Photoelectron Spectroscopy. X-ray photoelectron spectroscopy (XPS) was carried out to characterize the surface of the NP-Sn. The survey scan in Figure S3 indicates

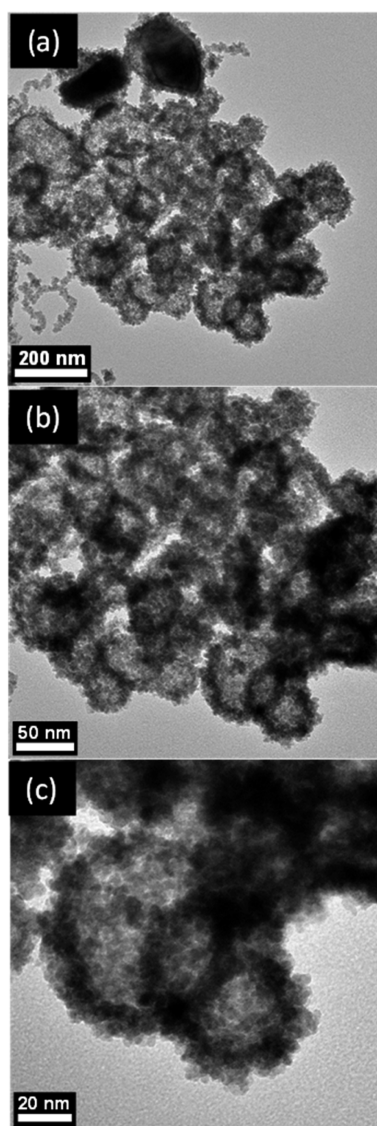


Figure 3. Transmission electron microscopy images of NP-Sn at different magnifications (a–c). The images indicate that the ligaments that are the primary building block of this hierarchical structure, are themselves porous, and are constructed from small nanoparticles. The 3D interconnections of these ligaments form the secondary pore structure of the NP-Sn architecture, resulting in a hierarchical porous architecture.

the presence of Sn, oxygen, carbon, and magnesium. Figure 4a shows the high-resolution XPS spectrum of the Sn $3d_{3/2}$ and $3d_{5/2}$ signals, which are fitted and assigned to three different chemical states. The binding energy of the $3d_{5/2}$ peak at 485.4 and 488.0 eV agrees well with metallic Sn⁴⁹ and SnO₂,⁵⁰ respectively. The peak at 490.2 eV and its pair at 498.7 can be assigned to SnO₃²⁻ or H₂SnO₃-type species.⁵¹ The surface of our NP-Sn likely contains insoluble stannic acid related species, which were produced from the reaction of tin and the acidic corrosion media. Typically bulk stannic acid is produced from the reaction of hot nitric acid and tin, so it is reasonable that some surface species could be similarly created here.⁵²

Figure 4b shows the high-resolution O 1s spectrum, which is fit with two peaks at 530.0 and 533.3 eV. The peak at lower binding energy corresponds to oxygen in tin oxide, while the peak at higher binding energy is associated with MgO,

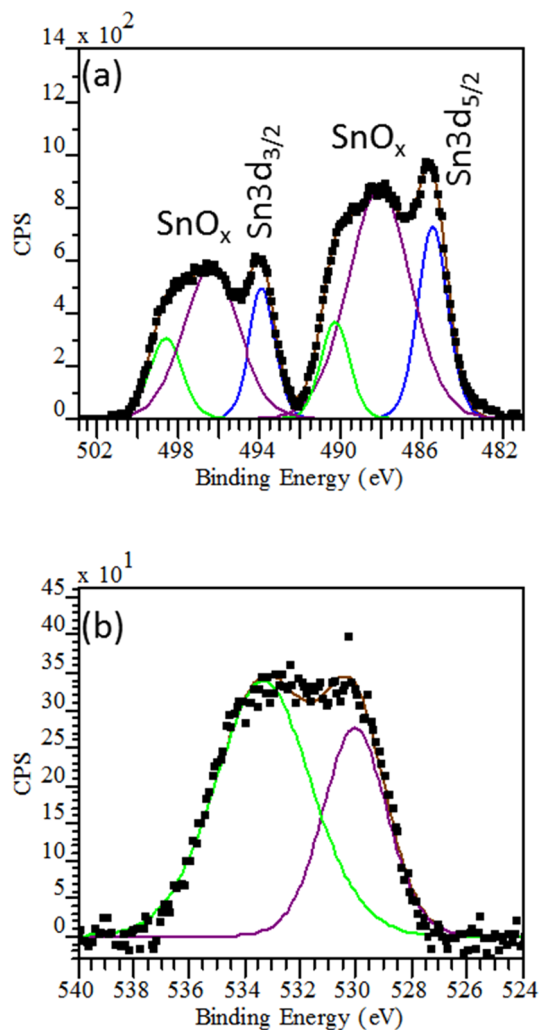


Figure 4. High-resolution XPS spectra showing the Sn 3d region (a) and the O 1s region (b). XPS has a very shallow penetration depth, so the presence of both tin metal and tin oxide in the XPS spectra indicates that the surface of the NP-Sn is covered with only a thin oxide layer. That layer is likely converted to tin and Li₂O during the first lithiation cycle.

Mg(OH)₂ and MgCO₃.^{53,54} Given the low penetration depth of XPS, the presence of both metallic Sn and tin oxide in the XPS spectra indicates that the surface of the material is covered with only a thin tin oxide layer, which is likely reduced to Li₂O and Sn during the first electrochemical cycle.

3.4. Electrochemical Performance. The electrochemical properties of NP-Sn were evaluated in composite electrodes consisting of NP-Sn active material, vapor-grown carbon fibers (VGCFs), and carboxymethyl cellulose (CMC) binder. Previous studies have shown that VGCFs form continuous conductive pathways more easily than carbon black nanoparticles, and can even help increase cycle lifetimes of conversion-type and alloy-type electrodes.⁴⁵ CMC binder has also been shown to improve cycle lifetimes of alloy-type composite electrode, and adventitiously it is also water-soluble.⁴⁵ This formulation effectively eliminates the need for *n*-methyl-2-pyrrolidone, which is an expensive and toxic cosolvent used in Li-ion composite electrodes.⁵⁵ Figure S4 shows an SEM cross section of a thick composite electrode illustrating the interwoven network of carbon fibers. The network accommodates any further volume expansion of the

NP-Sn not already accommodated by the porous Sn architecture.

The electrochemistry of the NP-Sn half-cells was investigated using galvanostatic measurements. One high current activation cycle (insertion and deinsertion at 1 A/g or 1.5C) was performed over the voltage range from the OCV of the as-synthesized Sn (2.6–2.4 V vs Li/Li⁺) down to 0.07 V and then back up to 1 V. This activation pulse reduces SnO₂ on the surface of NP-Sn, converting it to Sn and Li₂O. Pure tin metal has been shown to catalyze electrolyte decomposition above 1.5 V, however, which leads to premature electrode failure.⁵⁶ Because the majority phase in NP-Sn is tin metal, the activation pulse is used to rapidly lower the voltage to prevent the formation of a thick solid electrode interphase (SEI) layer.⁵⁶

The ideas discussed above are also confirmed by electrochemical impedance spectroscopy (Figure 5), which shows that

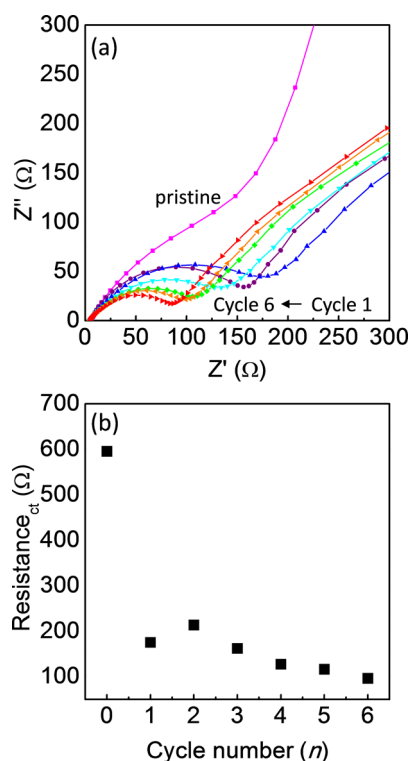


Figure 5. Nyquist plots of the first six cycles of a NP-Sn electrode recorded at 1.0 V after a 60 s rest (a). Charge transfer resistance calculated from the midfrequency semicircle region of the Nyquist plots (b). These data show that the charge transfer resistance significantly decreases as the thin tin oxide surface layer on the NP-Sn is reduced.

the charge transfer resistance decreases significantly after the first activation cycle, and continues to decrease during the first 5 cycles. The initial drop in charge transfer resistance may be attributed to the conversion of the poorly conducting SnO_x (0 < x ≤ 2) surface layer to a more conductive interphase layer. The small increase in resistance for cycle 2 is likely a result of further SEI formation, which will increase the charge transfer resistance. The decrease in resistance between cycles 3–6 could be due to increased electrolyte penetration into confined pores, or restructuring of the porous Sn to increase solvent diffusion or electrical conductivity. Overall, the impedance drops significantly during the first cycle, but remains fairly constant thereafter.

Figure 6a shows the capacity versus voltage curves of NP-Sn collected at 250 mA/g (0.38C). These curves show several plateaus that are indicative of two phase reactions between Li_xSn_y phases.⁵⁷ The first cycle coulombic efficiency (after the formation cycle) of the NP-Sn based material is 70%, which is similar to or better than other Sn-based electrodes reported in the literature.^{19,22} We also measured the first cycle coulombic efficiency at a low current density of 100 mA/g (0.15C) and found very similar values for the coulombic efficiency (67%). While the first cycle coulombic efficiency is modest, the XPS and EDS analyses indicate that only a small amount of tin exists as tin oxide. The low oxygen content, in turn, indicates that the total SnO₂ fraction in the material is also low. The irreversibility of the first cycle is thus likely a combination of some surface SnO₂ reduction and SEI formation, with the dominant process likely being SEI formation, as expected for a high surface area nanostructured electrode material.^{19,22}

Upon further cycling, the coulombic efficiency quickly increases to 97% after three cycles, which suggests that the SEI layer formed during these first few cycles is stable, and that parasitic side reactions have largely been passivated. It will be shown in the following section that the porous architecture enables this NP-Sn material to expand without cracking, which is a typical failure mechanism that leads to uncontrolled growth of the SEI layer and ultimately cell failure. In Table 1 we compare our work to other Sn- and SnO₂-based nanostructures. As we discussed in the Introduction, SnO₂ has an extremely low first cycle efficiency,^{27–29} and the improved first cycle coulombic efficiency of our NP-Sn (Table 1) illustrates the benefit of designing tin metal nanostructures (NP-Sn) rather than SnO₂-based nanostructures.

Beyond issues of first cycle efficiency, Figure 6b shows the extended cycling performance of NP-Sn at 250 mA/g (0.38C). A capacity increase during the first 5 cycles of 12% from 578 to 658 mAh/g is observed, and is correlated to the decrease in charge transfer resistance measured by impedance spectroscopy over the same interval (see Figure 5). Near the 70th cycle, the capacity reaches a maximum value of 693 mAh/g, and the capacity only starts to slowly decay after 150 cycles. After nearly 300 cycles, 80% of the maximum capacity remains (555 mAh/g), which is an excellent demonstration of the practical ability of this nanoscale architecture to accommodate the volume change that occurs during alloying. Again, Table 1 illustrates the excellent cycle lifetime of NP-Sn as compared to other state of the art nanostructured Sn and SnO₂ materials.

We note that most studies only report lifetimes of 100 cycles or below, while our NP-Sn was cycled 350 times. To make a more direct comparison with these shorter lifetime tests, a capacity decay rate was calculated from the data in Table 1. We define this decay rate as the total discharge capacity loss, normalized by the number of cycles (mAh/g/cycle). The decay rate of our NP-Sn is significantly lower than that of other materials in this table, illustrating again the excellent reversibility of the NP-Sn. This table is not meant to be an exhaustive list, but is provided to understand the impact of our work. For a more extensive list of the cycling performance of tin, several reviews have been published.^{17,18}

As discussed above, it is believed that the microscopic morphology of the electrode at the nano/meso scale plays a key role in the electrochemical cycling and affects the battery lifetime significantly. For direct three-dimensional (3D) visualization of the battery electrode, we performed transmission X-ray microscopy to examine electrodes recovered

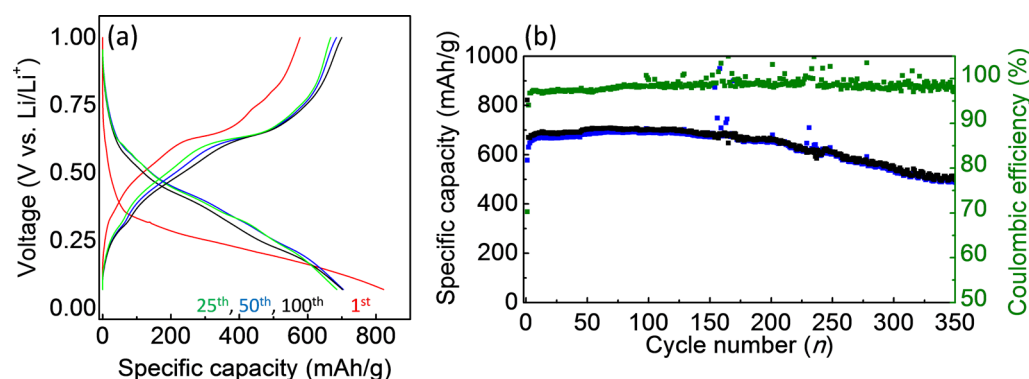


Figure 6. Voltage as a function of capacity for NP-Sn at a current density of 250 mA/g (0.38C) (a). Red, green, blue, and black traces correspond to the 1st, 25th, 50th, and 100th cycles, respectively. Capacity and coulombic efficiency recorded at 250 mA/g as a function of the cycle number showing the long cycle lifetime (b). Charge curves are shown in black, while discharge is in blue. One high current activation cycle (insertion and deinsertion at 1 A/g or 1.5C) was performed over the voltage range from the OCV of the as-synthesized Sn (2.6–2.4 V vs Li/Li⁺) down to 0.07 V and then back up to 1 V prior to long-term cycling.

Table 1. Electrochemical Performance Data of Nanostructured Sn and SnO₂

material type	first charge capacity (mAh/g), rate (A/g)	first discharge capacity (mAh/g), rate (A/g)	first cycle coulombic efficiency (%)	reversible capacity after <i>n</i> cycles (mAh/g), rate (A/g)	decay rate (mAh/g/cycle)	ref
NP-Sn	932, 0.100	628, 0.100	67	350, 500, 0.250	0.366	this work
Sn nanoparticles	1580, 0.099	880, 0.099	56	70, 700, 0.099	2.57	20
interconnected SnO ₂ super lattice	1570, 0.600	676, 0.600	43	100, 600, ^a 0.600	0.760 ^b	26
ordered porous SnO ₂	1650, ^a 0.078	800, ^a 0.078	48	100, 564, 0.391	2.36	27
highly porous SnO ₂ nanotubes	1781, 0.100	937, 0.100	53	50, 645, 0.100	5.84	68
hollow SnO ₂ nanostructures	1602, 0.100	878, 0.100	55	50, 545, 0.100	6.66	69

^aIndicates value estimated from a published graph. ^bThe decay rate was calculated from the capacity at the 100th cycle rather than the 200th cycle, because the capacity increases from ~600 to ~650 mAh/g between the 100th and 200th cycles.

from a series of battery cells at different cycling stages.^{58–61} The resolution of this microscope used to image NP-Sn is ~30 nm, so we are only able to image pores above this size. The smaller pores in the NP-Sn particles are effectively invisible with this microscope. While TEM could potentially be used to monitor this smaller porosity, it is limited to thin samples and frequently without electrolyte. The advantage of TXM is that the large penetration depth of X-rays allows for full imaging of single NP-Sn particles that are micrometers thick. Furthermore, the larger pores (>30 nm) in NP-Sn enable effective electrolyte accessibility throughout the entire grain, so monitoring these pores yields information about the electrolyte accessibility into the bulk of the NP-Sn particles at different states of charge.

The 3D renderings of the electrode at three different stages of the electrochemical cycling are shown in Figure 7. The tomography data in Figure 7a–c show that the micrometer-sized NP-Sn particles come in a wide distribution of sizes (1–20 μm), as was previously determined by SEM analysis. Figure 7d shows that the pristine particles consist of an interconnected network of random meso- and nanopores that arise from the dealloying process. The magnified views of NP-Sn at various states of charge (Figure 7d–f) show that both the Li₂₂Sn₅ (as confirmed by XRD in Figure S5) and the delithiated β-Sn remain porous with interconnected ligaments. Figure 7e is particularly important because it shows that even in the fully lithiated state, after a reported ~300% volume expansion, the initially detected random porosity and interconnected ligaments still remain. Several views of these 3D renderings,

at the three different states of charge, are provided as movies in the Supporting Information (M1–M3). These observations indicate that the porous architecture can accommodate the Li-induced expansion and contraction, while still preserving void space for electrolyte diffusion.

Previous transmission X-ray microscopy studies on bulk Sn have suggested that the major failure mechanism in tin-based electrodes is significant cracking during charge and discharge, which exposes fresh tin surfaces that can participate in further electrolyte decomposition.⁶² In turn, this insulating SEI layer increases the cell impedance and decreases the lifetime. In addition, the carbon electrode matrix significantly deforms during the expansion process, leading to Sn that is electronically isolated from the conductive matrix.⁶² Combining the observation that porosity is retained at both charged and discharged states in TXM, and the long-term cycling stability, seems to indicate that extreme volume change is reduced significantly in this system. This observation is in good agreement with the idea that a porous morphology at the nano/meso scale provides a positive impact on the battery cycling lifetime.^{25–29,31,63}

We would like to point out that the material described here does not achieve the full theoretical capacity associated with the Li₂₂Sn₅ phase, which corresponds to a capacity of 990 mAh/g. The maximum capacity achieved for NP-Sn is 693 mAh/g. Part of the capacity is sacrificed by limiting the lower voltage cutoff to 70 mV. Previous studies have shown that underpotential Li deposition occurs on graphite surfaces at potentials below 70

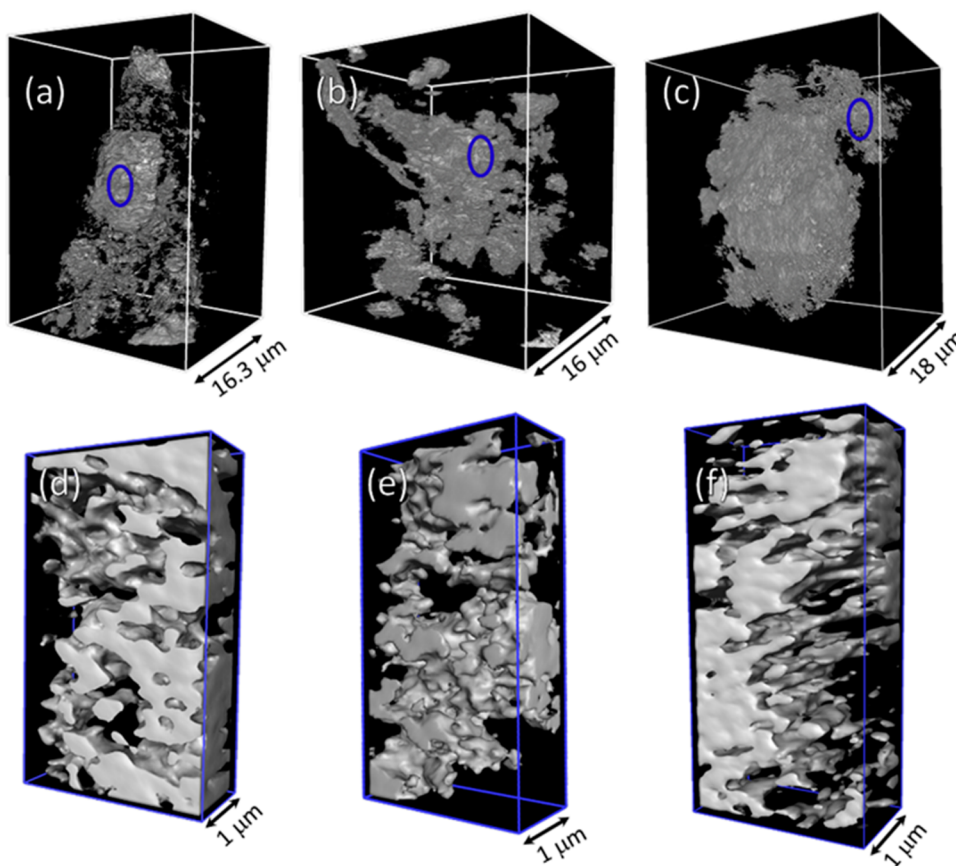


Figure 7. Three-dimensional visualization of the nano/meso structure of the Sn electrode at different cycling stages. Panel (a) shows the pristine sample; panel (b) is the electrode recovered after one electrochemical cycle at 1.2 V; and panel (c) shows the fully lithiated sample at 70 mV. Panels (d), (e), and (f) show the magnified isosurface renderings of the highlighted areas in panels (a), (b), and (c), respectively. The scale of each volume is indicated in the panels.

mV, especially at fast rates, which can negatively affect the cycle lifetime.^{64,65} Even with the relatively high 70 mV cut off voltage, however, the $\text{Li}_{22}\text{Sn}_5$ phase is still formed (Figure S5). The $\text{Li}_{22}\text{Sn}_5$ phase (2.05 g/cm^3) is markedly lower in density than the $\beta\text{-Sn}$ phase (7.3 g/cm^3), and conversion to this phase represents the largest volume change during the electrochemical lithiation.⁸ The data presented in this Article thus suggest that the improved electrochemical performance shown here is achieved by controlling material properties, and not by artificially preventing the formation of $\text{Li}_{22}\text{Sn}_5$ through control of the lower voltage cut off.

Additional capacity reduction also results from the $\sim 5\%$ of magnesium that remains in the final material, as confirmed by XRD and EDS (Figure 1). Any additional discrepancies between the theoretical capacity and our observed capacity must be assigned to small parts of the material that are electrochemically inactive, either because they are electrically isolated, or because the pores are blocked and they are inaccessible to the electrolyte. Despite these issues, the capacity of 693 mAh/g achieved in this work represents a near doubling of the specific capacity of graphite used in commercial applications.

Even though most works on high-performance battery anodes concentrate on achieving very high gravimetric capacities, in practical Li-ion batteries, anode capacities above 1000 mAh/g add very little to the total energy density of the full battery due to electrode capacity matching considerations.⁶⁶ As a result, tripling or quadrupling the gravimetric capacity of an anode material does not lead to the same magnification in

total cell capacity. Volumetric energy density, on the other hand, is an extremely important metric because of the size limitations in most end-use applications. In comparison to graphite, tin has a nearly 3-fold higher theoretical volumetric capacity as compared to graphite.⁶⁷ The calculated volumetric capacity of the NP-Sn electrode material shown is 870 mAh/cm^3 , which is double the value of commercial graphite slurry electrodes.⁶ See Table S1 for details on the volumetric energy calculations. This increased volumetric capacity could have a significant effect on the reduction in overall size of a full cell battery.

Finally, the kinetic performance of NP-Sn was investigated through galvanostatic charge and discharge from 100 mA/g (0.15C) to 1000 mA/g (1.5C). Figure 8a and b shows that the charge storage capacity of NP-Sn is nearly independent of rate between 100 and 500 mA/g (0.15–0.77C), retaining over 93% of the original capacity at 500 mA/g (0.77C). Even at 1 A/g (1.5C), 545 mAh/g can be accessed, which is 3-fold higher than graphite at the same current density.³ We speculate that the fast kinetics arise from the synergistic effects of the hierarchical electrode structure. That is to say, the porous Sn powder consists of interconnected nanograins that are electrically well connected to the macroporous carbon fiber electrode network. The interplay between that ideal porosity across multiple length scales and a highly electrically conducting network enables this NP-Sn system to undergo extremely fast charge transfer.

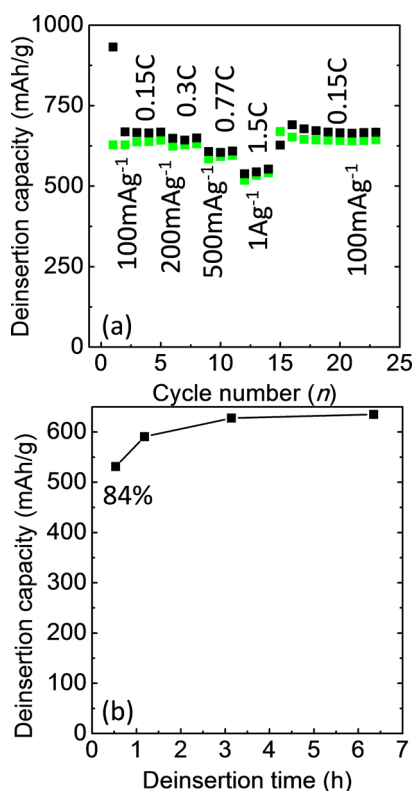


Figure 8. Capacity of NP-Sn as a function of cycle number at different current densities (a). Charge data are shown in black, while discharge is in green. Discharge capacity of NP-Sn as a function of the deinsertion time (b).

4. CONCLUSIONS

Micrometer-sized grains of nanoporous Sn have been synthesized through a simple and scalable selective alloy corrosion method. The ligament morphology in the nanoporous Sn is comprised of aggregated nanoparticles, rather than the more widely observed interconnected nanowire-like morphology. When used as an anode materials in a Li half-cell, Sn metal with this porous architecture exhibits long cycle lifetimes of over 350 cycles. Synchrotron-based ex situ X-ray tomography was used to examine the origins of the markedly improved cycling lifetimes. This experiment has led to the understanding that the novel nanoporous Sn architecture is preserved in the lithiated state and helps to accommodate the extreme volume expansion during cycling. Besides the long cycle lifetimes, good kinetic performance is exhibited by the nanoporous Sn powder. At a current density of 1 A/g (1.5C), over 84% of the initial capacity is recovered.

This work thus demonstrates that nanoporous metals are ideal architectures for alloy-type electrochemical energy storage materials. This favorable behavior is enabled by the fact that nanoporous metals exhibit a very good intrinsic electrical conductivity, and, at the same time, they are able to accommodate the Li storage-induced volume change.

■ ASSOCIATED CONTENT

Supporting Information

The Supporting Information is available free of charge on the ACS Publications website at DOI: 10.1021/acsami.6b09014.

Adsorption and desorption isotherms, calculated pore size distribution, XPS survey scan, electrode cross-section

image, ex situ XRD plot after cycling, and table with parameters used to calculate volumetric capacity (PDF) Movie of a 3D reconstruction obtained from TXM of a pristine single particle before cycling (MPG) Movie of a 3D reconstruction obtained from TXM of a single particle after full alloying with Li (MPG) Movie of a 3D reconstruction obtained from TXM of a single particle after the first discharge to recover pure Sn from the Li/Sn alloy (MPG)

■ AUTHOR INFORMATION

Corresponding Author

*E-mail: tolbert@chem.ucla.edu.

ORCID

Sarah H. Tolbert: 0000-0001-9969-1582

Author Contributions

[†]J.B.C. and E.D. contributed equally to this work.

Notes

The authors declare no competing financial interest.

■ ACKNOWLEDGMENTS

The Netherlands Organization for Scientific Research (NWO-The Hague, Rubicon Grant Dossier nr: 680-50-1214) is thanked for its financial support. Support for this work was provided by the U.S. Department of Energy (DOE) under award DE-SC0014213 (structural characterization, electrochemical measurements, electrode fabrication, and some materials synthesis) and by the UCLA Physical Science Innovation and Entrepreneurship Fund (additional materials synthesis and fabrication). Additional support for electron microscopy was provided by the Office of Naval Research. Use of the Stanford Synchrotron Radiation Lightsource, SLAC National Accelerator Laboratory, is supported by the U.S. Department of Energy, Office of Science, Office of Basic Energy Sciences, under contract no. DE-AC02-76SF00515. Engineering support from Dr. D. Van Campen for the TXM experiment at beamline 6-2C of SSRL is gratefully acknowledged.

■ REFERENCES

- (1) Scrosati, B. Lithium Rocking Chair Batteries: An Old Concept? *J. Electrochem. Soc.* **1992**, *139*, 2776–2781.
- (2) Ozawa, K. Lithium-Ion Rechargeable Batteries with LiCoO₂ and Carbon Electrodes: The LiCoO₂/C System. *Solid State Ionics* **1994**, *69*, 212–221.
- (3) Sivakkumar, S. R.; Nerkar, J. Y.; Pandolfo, A. G. Rate Capability of Graphite Materials as Negative Electrodes in Lithium-Ion Capacitors. *Electrochim. Acta* **2010**, *55*, 3330–3335.
- (4) Endo, M.; Kim, C.; Nishimura, K.; Fujino, T.; Miyashita, K. Recent Development of Carbon Materials for Li Ion Batteries. *Carbon* **2000**, *38*, 183–197.
- (5) Sivakkumar, S. R.; Milev, A. S.; Pandolfo, A. G. Effect of Ball-Milling on the Rate and Cycle-Life Performance of Graphite as Negative Electrodes in Lithium-Ion Capacitors. *Electrochim. Acta* **2011**, *56*, 9700–9706.
- (6) Thakur, M.; Pernites, R. B.; Nitta, N.; Isaacson, M.; Sinsabaugh, S. L.; Wong, M. S.; Biswal, S. L. Freestanding Macroporous Silicon and Pyrolyzed Polyacrylonitrile As a Composite Anode for Lithium Ion Batteries. *Chem. Mater.* **2012**, *24*, 2998–3003.
- (7) Larcher, D.; Beattie, S.; Morcrette, M.; Edström, K.; Jumas, J.-C.; Tarascon, J.-M. Recent Findings and Prospects in the Field of Pure Metals as Negative Electrodes for Li-Ion Batteries. *J. Mater. Chem.* **2007**, *17*, 3759–3772.

- (8) Courtney, I. A.; Dahn, J. R. Electrochemical and In Situ X-Ray Diffraction Studies of the Reaction of Lithium with Tin Oxide Composites. *J. Electrochem. Soc.* **1997**, *144*, 2045–2052.
- (9) Huggins, R. A.; Nix, W. D. Decrepitation Model for Capacity Loss during Cycling of Alloys in Rechargeable Electrochemical Systems. *Ionics* **2000**, *6*, 57–63.
- (10) Beaulieu, L. Y.; Eberman, K. W.; Turner, R. L.; Krause, L. J.; Dahn, J. R. Colossal Reversible Volume Changes in Lithium Alloys. *Electrochem. Solid-State Lett.* **2001**, *4*, A137–A140.
- (11) Park, C.-M.; Kim, J.-H.; Kim, H.; Sohn, H.-J. Li-Alloy Based Anode Materials for Li Secondary Batteries. *Chem. Soc. Rev.* **2010**, *39*, 3115–3141.
- (12) Besenhard, J. O.; Yang, J.; Winter, M. Will Advanced Lithium-Alloy Anodes Have a Chance in Lithium-Ion Batteries? *J. Power Sources* **1997**, *68*, 87–90.
- (13) Huang, J. Y.; Zhong, L.; Wang, C. M.; Sullivan, J. P.; Xu, W.; Zhang, L. Q.; Mao, S. X.; Hudak, N. S.; Liu, X. H.; Subramanian, A.; Fan, H.; Qi, L.; Kushima, A.; Li, J. In Situ Observation of the Electrochemical Lithiation of a Single SnO₂ Nanowire Electrode. *Science* **2010**, *330*, 1515–1521.
- (14) He, Y.; Yu, X.; Li, G.; Wang, R.; Li, H.; Wang, Y.; Gao, H.; Huang, X. Shape Evolution of Patterned Amorphous and Polycrystalline Silicon Microarray Thin Film Electrodes Caused by Lithium Insertion and Extraction. *J. Power Sources* **2012**, *216*, 131–138.
- (15) Liu, X. H.; Zheng, H.; Zhong, L.; Huang, S.; Karki, K.; Zhang, L. Q.; Liu, Y.; Kushima, A.; Liang, W. T.; Wang, J. W.; Cho, J.-H.; Epstein, E.; Dayeh, S. A.; Picraux, S. T.; Zhu, T.; Li, J.; Sullivan, J. P.; Cumings, J.; Wang, C.; Mao, S. X.; Ye, Z. Z.; Zhang, S.; Huang, J. Y. Anisotropic Swelling and Fracture of Silicon Nanowires during Lithiation. *Nano Lett.* **2011**, *11*, 3312–3318.
- (16) Goriparti, S.; Miele, E.; Angelis, F. D.; Fabrizio, E. D.; Zaccaria, R. P.; Capiglia, C. Review on Recent Progress of Nanostructured Anode Materials for Li-Ion Batteries. *J. Power Sources* **2014**, *257*, 421–443.
- (17) Deng, Y.; Fang, C.; Chen, G. The Developments of SnO₂/graphene Nanocomposites as Anode Materials for High Performance Lithium Ion Batteries: A Review. *J. Power Sources* **2016**, *304*, 81–101.
- (18) Liu, L.; Xie, F.; Lyu, J.; Zhao, T.; Li, T.; Choi, B. G. Tin-Based Anode Materials with Well-Designed Architectures for next-Generation Lithium-Ion Batteries. *J. Power Sources* **2016**, *321*, 11–35.
- (19) Xu, L.; Kim, C.; Shukla, A. K.; Dong, A.; Mattox, T. M.; Milliron, D. J.; Cabana, J. Monodisperse Sn Nanocrystals as a Platform for the Study of Mechanical Damage during Electrochemical Reactions with Li. *Nano Lett.* **2013**, *13*, 1800–1805.
- (20) Im, H. S.; Cho, Y. J.; Lim, Y. R.; Jung, C. S.; Jang, D. M.; Park, J.; Shojaei, F.; Kang, H. S. Phase Evolution of Tin Nanocrystals in Lithium Ion Batteries. *ACS Nano* **2013**, *7*, 11103–11111.
- (21) Xu, Y.; Liu, Q.; Zhu, Y.; Liu, Y.; Langrock, A.; Zachariah, M. R.; Wang, C. Uniform Nano-Sn/C Composite Anodes for Lithium Ion Batteries. *Nano Lett.* **2013**, *13*, 470–474.
- (22) Ding, L.; He, S.; Miao, S.; Jorgensen, M. R.; Leubner, S.; Yan, C.; Hickey, S. G.; Eychmüller, A.; Xu, J.; Schmidt, O. G. Ultrasmall SnO₂ Nanocrystals: Hot-Bubbling Synthesis, Encapsulation in Carbon Layers and Applications in High Capacity Li-Ion Storage. *Sci. Rep.* **2014**, *4*, 1–8.
- (23) Li, J.; Wu, P.; Ye, Y.; Wang, H.; Zhou, Y.; Tang, Y.; Lu, T. Designed Synthesis of SnO₂ @C Yolk-shell Spheres for High-Performance Lithium Storage. *CrystEngComm* **2014**, *16*, 517–521.
- (24) Deng, D.; Kim, M. G.; Lee, J. Y.; Cho, J. Green Energy Storage Materials: Nanostructured TiO₂ and Sn-Based Anodes for Lithium-Ion Batteries. *Energy Environ. Sci.* **2009**, *2*, 818–837.
- (25) Ba, J.; Polleux, J.; Antonietti, M.; Niederberger, M. Non-Aqueous Synthesis of Tin Oxide Nanocrystals and Their Assembly into Ordered Porous Mesostructures. *Adv. Mater.* **2005**, *17*, 2509–2512.
- (26) Jiao, Y.; Han, D.; Ding, Y.; Zhang, X.; Guo, G.; Hu, J.; Yang, D.; Dong, A. Fabrication of Three-Dimensionally Interconnected Nanoparticle Superlattices and Their Lithium-Ion Storage Properties. *Nat. Commun.* **2015**, *6*, 1–8.
- (27) Etacheri, V.; Seisenbaeva, G. A.; Caruthers, J.; Daniel, G.; Nedelec, J.-M.; Kessler, V. G.; Pol, V. G. Ordered Network of Interconnected SnO₂ Nanoparticles for Excellent Lithium-Ion Storage. *Adv. Energy Mater.* **2015**, *5*, 1401289.
- (28) Ge, M.; Fang, X.; Rong, J.; Zhou, C. Review of Porous Silicon Preparation and Its Application for Lithium-Ion Battery Anodes. *Nanotechnology* **2013**, *24*, 1–10.
- (29) Kim, H.; Han, B.; Choo, J.; Cho, J. Three-Dimensional Porous Silicon Particles for Use in High-Performance Lithium Secondary Batteries. *Angew. Chem., Int. Ed.* **2008**, *47*, 10151–10154.
- (30) Yu, Y.; Gu, L.; Zhu, C.; Tsukimoto, S.; van Aken, P. A.; Maier, J. Reversible Storage of Lithium in Silver-Coated Three-Dimensional Macroporous Silicon. *Adv. Mater.* **2010**, *22*, 2247–2250.
- (31) Jia, H.; Gao, P.; Yang, J.; Wang, J.; Nuli, Y.; Yang, Z. Novel Three-Dimensional Mesoporous Silicon for High Power Lithium-Ion Battery Anode Material. *Adv. Energy Mater.* **2011**, *1*, 1036–1039.
- (32) Erlebacher, J.; Aziz, M. J.; Karma, A.; Dimitrov, N.; Sieradzki, K. Evolution of Nanoporosity in Dealloying. *Nature* **2001**, *410*, 450–453.
- (33) Chapman, C. A. R.; Daggumati, P.; Gott, S. C.; Rao, M. P.; Seker, E. Substrate Topography Guides Pore Morphology Evolution in Nanoporous Gold Thin Films. *Scr. Mater.* **2016**, *110*, 33–36.
- (34) Detsi, E.; Punzhin, S.; Rao, J.; Onck, P. R.; De Hosson, J. T. M. Enhanced Strain in Functional Nanoporous Gold with a Dual Microscopic Length Scale Structure. *ACS Nano* **2012**, *6*, 3734–3744.
- (35) Detsi, E.; Vuković, Z.; Punzhin, S.; Bronsveld, P. M.; Onck, P. R.; Hosson, J. T. M. De Fine-Tuning the Feature Size of Nanoporous Silver. *CrystEngComm* **2012**, *14*, 5402–5406.
- (36) Hodge, A. M.; Biener, J.; Hayes, J. R.; Bythrow, P. M.; Volkert, C. A.; Hamza, A. V. Scaling Equation for Yield Strength of Nanoporous Open-Cell Foams. *Acta Mater.* **2007**, *55*, 1343–1349.
- (37) Li, W. C.; Balk, T. J. Preparation and Hydrogen Absorption/desorption of Nanoporous Palladium Thin Films. *Materials* **2009**, *2*, 2496–2509.
- (38) Sun, Y.; Ye, J.; Shan, Z.; Minor, A. M.; Balk, T. J. The Mechanical Behavior of Nanoporous Gold Thin Films. *JOM* **2007**, *59*, 54–58.
- (39) Detsi, E.; Van De Schootbrugge, M.; Punzhin, S.; Onck, P. R.; De Hosson, J. T. M. On Tuning the Morphology of Nanoporous Gold. *Scr. Mater.* **2011**, *64*, 319–322.
- (40) Jin, H. J.; Wang, X. L.; Parida, S.; Wang, K.; Seo, M.; Weissmüller, J. Nanoporous Au-Pt Alloys as Large Strain Electrochemical Actuators. *Nano Lett.* **2010**, *10*, 187–194.
- (41) Chen, Q.; Sieradzki, K. Spontaneous Evolution of Bicontinuous Nanostructures in Dealloyed Li-Based Systems. *Nat. Mater.* **2013**, *12*, 1102–1106.
- (42) Balk, T. J.; Eberl, C.; Sun, Y.; Hemker, K. J.; Gianola, D. S. Tensile and Compressive Microspecimen Testing of Bulk Nanoporous Gold. *JOM* **2009**, *61*, 26–31.
- (43) Hakamada, M.; Mabuchi, M. Preparation of Nanoporous Ni and Ni-Cu by Dealloying of Rolled Ni-Mn and Ni-Cu-Mn Alloys. *J. Alloys Compd.* **2009**, *485*, 583–587.
- (44) Hakamada, M.; Mabuchi, M. Nanoporous Nickel Fabricated by Dealloying of Rolled Ni-Mn Sheet. *Procedia Eng.* **2014**, *81*, 2159–2164.
- (45) Lestriez, B.; Desaeve, S.; Danet, J.; Moreau, P.; Plée, D.; Guyomard, D. Hierarchical and Resilient Conductive Network of Bridged Carbon Nanotubes and Nanofibers for High-Energy Si Negative Electrodes. *Electrochem. Solid-State Lett.* **2009**, *12*, A76–A80.
- (46) Liu, Y.; Meier, F.; Williams, P. A.; Wang, J.; Andrews, J. C.; Pianetta, P. TXM-Wizard: A Program for Advanced Data Collection and Evaluation in Full-Field Transmission X-Ray Microscopy. *J. Synchrotron Radiat.* **2012**, *19*, 281–287.
- (47) Detsi, E.; Punzhin, S.; Onck, P. R.; De Hosson, J. T. M. Direct Synthesis of Metal Nanoparticles with Tunable Porosity. *J. Mater. Chem.* **2012**, *22*, 4588–4591.
- (48) Detsi, E.; Onck, P.; De Hosson, J. T. M. Metallic Muscles at Work: High Rate Actuation in Nanoporous Gold/polyaniline Composites. *ACS Nano* **2013**, *7*, 4299–4306.

(49) Baronetti, G. T.; Miguel, S. R.; Scelza, O. A.; Castro, A. A. State of Metallic Phase in Pt-Sn/Al₂O₃ Catalysts Prepared by Different Deposition Techniques. *Appl. Catal.* **1986**, *24*, 109–116.

(50) Süzer, S.; Voskoboinikov, T.; Hallam, K. R.; Allen, G. C. Electron Spectroscopic Investigation of Sn Coatings on Glasses. *Anal. Bioanal. Chem.* **1996**, *355*, 654–656.

(51) Dai, H.-B.; Ma, G.-L.; Xia, H.-J.; Wang, P. Reaction of Aluminium with Alkaline Sodium Stannate Solution as a Controlled Source of Hydrogen. *Energy Environ. Sci.* **2011**, *4*, 2206–2212.

(52) Posnjak, E. The Nature of Stannic Acids. *J. Phys. Chem.* **1925**, *30*, 1073–1077.

(53) Yang, J.; Yim, C. D.; You, B. S. Effects of Sn in α -Mg Matrix on Properties of Surface Films of Mg-xSn (X = 0, 2, 5 Wt%) Alloys. *Mater. Corros.* **2016**, *67*, 531–541.

(54) Liu, X.; Shan, D.; Song, Y.; Chen, R.; Han, E. Influences of the Quantity of Mg₂Sn Phase on the Corrosion Behavior of Mg-7Sn Magnesium Alloy. *Electrochim. Acta* **2011**, *56*, 2582–2590.

(55) Wood, D. L.; Li, J.; Daniel, C. Prospects for Reducing the Processing Cost of Lithium Ion Batteries. *J. Power Sources* **2015**, *275*, 234–242.

(56) Beattie, S. D.; Hatchard, T.; Bonakdarpour, A.; Hewitt, K. C.; Dahn, J. R. Anomalous, High-Voltage Irreversible Capacity in Tin Electrodes for Lithium Batteries. *J. Electrochem. Soc.* **2003**, *150*, A701–A705.

(57) Rhodes, K. J.; Meisner, R.; Kirkham, M.; Dudney, N.; Daniel, C. In Situ XRD of Thin Film Tin Electrodes for Lithium Ion Batteries. *J. Electrochem. Soc.* **2012**, *159*, A294–A299.

(58) Weker, J. N.; Liu, N.; Misra, S.; Andrews, J. C.; Cui, Y.; Toney, M. F. In Situ Nanotomography and Operando Transmission X-Ray Microscopy of Micron-Sized Ge Particles. *Energy Environ. Sci.* **2014**, *7*, 2771–2777.

(59) Weker, J. N.; Toney, M. F. Emerging In Situ and Operando Nanoscale X-Ray Imaging Techniques for Energy Storage Materials. *Adv. Funct. Mater.* **2015**, *25*, 1622–1637.

(60) Nelson, J.; Misra, S.; Yang, Y.; Jackson, A.; Liu, Y.; Wang, H.; Dai, H.; Andrews, J. C.; Cui, Y.; Toney, M. F.; Andrews, J. C. In Operando X-Ray Diffraction and Transmission X-Ray Microscopy of Lithium Sulfur Batteries In Operando X-Ray Diffraction and Transmission X-Ray Microscopy of Lithium Sulfur Batteries. *J. Am. Chem. Soc.* **2012**, *134*, 6337–6343.

(61) Lin, F.; Nordlund, D.; Weng, T.-C.; Zhu, Y.; Ban, C.; Richards, R. M.; Xin, H. L. Phase Evolution for Conversion Reaction Electrodes in Lithium-Ion Batteries. *Nat. Commun.* **2014**, *5*, 1–9.

(62) Chao, S. C.; Song, Y. F.; Wang, C. C.; Sheu, H. S.; Wu, H. C.; Wu, N. L. Study on Microstructural Deformation of Working Sn and SnSb Anode Particles for Li-Ion Batteries by in Situ Transmission X-Ray Microscopy. *J. Phys. Chem. C* **2011**, *115*, 22040–22047.

(63) Nishio, K.; Tagawa, S.; Fukushima, T.; Masuda, H. Highly Ordered Nanoporous Si for Negative Electrode of Rechargeable Lithium-Ion Battery. *Electrochem. Solid-State Lett.* **2012**, *15*, A41–A44.

(64) Lu, W.; López, C. M.; Liu, N.; Vaughey, J. T.; Jansen, A.; Dees, D. W. Overcharge Effect on Morphology and Structure of Carbon Electrodes for Lithium-Ion Batteries. *J. Electrochem. Soc.* **2012**, *159*, A566–A570.

(65) Harris, S. J.; Timmons, A.; Baker, D. R.; Monroe, C. Direct in Situ Measurements of Li Transport in Li-Ion Battery Negative Electrodes. *Chem. Phys. Lett.* **2010**, *485*, 265–274.

(66) Zhang, W. J. A Review of the Electrochemical Performance of Alloy Anodes for Lithium-Ion Batteries. *J. Power Sources* **2011**, *196*, 13–24.

(67) Nitta, N.; Yushin, G. High-Capacity Anode Materials for Lithium-Ion Batteries: Choice of Elements and Structures for Active Particles. *Part. Part. Syst. Charact.* **2014**, *31*, 317–336.

(68) Yang, T.; Lu, B. Highly Porous Structure Strategy to Improve the SnO₂ Electrode Performance for Lithium-Ion Batteries. *Phys. Chem. Chem. Phys.* **2014**, *16*, 4115–4121.

(69) Yin, X. M.; Li, C. C.; Zhang, M.; Hao, Q. Y.; Liu, S.; Chen, L. B.; Wang, T. H. One-Step Synthesis of Hierarchical SnO₂ Hollow

Nanostructures via Self-Assembly for High Power Lithium Ion Batteries. *J. Phys. Chem. C* **2010**, *114*, 8084–8088.

NOTE ADDED AFTER ASAP PUBLICATION

This paper published ASAP on 12/22/2016. The erroneous compound LiO₂ was corrected to Li₂O and the revised version was reposted on 1/11/2017.